A non-linear homogeneous model for bone-like materials under compressive load.

M. Mengoni[1*], R. Voide[2], C. de Bien[3] , H. Freichels[4,†], C. Jérôme[4], A. Léonard[3],
D. Toye[3], R. Müller[2], G.H. van Lenthe[2,5], and J.P. Ponthot[1]

[1] *U. Liège, Department of Aerospace and Mechanics, LTAS - Non Linear Computational Mechanics, Liège, Belgium*
[2] *ETH Zürich, Institute for Biomechanics, Zürich, Switzerland*
[3] *U. Liège, Department of Applied Chemistry, Laboratory of Chemical Engineering, Liège, Belgium*
[4] *U. Liège, Center for Education and Research on Macromolecules, Liège, Belgium*
[5] *K.U. Leuven, Division of Biomechanics and Engineering Design, Leuven, Belgium*

SUMMARY

Finite element (FE) models accurately compute the mechanical response of bone and bone-like materials when the models include their detailed microstructure. In order to simulate non-linear behavior, which currently is only feasible at the expense of extremely high computational costs, coarser models can be used if the local morphology has been linked to the apparent mechanical behavior. The aim of this paper is to implement and validate such a constitutive law. This law is able to capture the non-linear structural behavior of bone-like materials through the use of fabric tensors. It also allows for irreversible strains using an elastoplastic material model incorporating hardening. These features are expressed in a constitutive law based on the anisotropic continuum damage theory coupled with isotropic elastoplasticity in a finite strains framework. This material model was implemented into Metafor, a non-linear FE software. The implementation was validated against experimental data of cylindrical samples subjected to compression. Three materials with bone-like microstructure were tested : aluminum foams of variable density (ERG, Oakland, CA), PLA (polylactic acid) foam (CERM, University of Liège) and cancellous bone tissue of a deer antler (Faculty of Veterinary Medicine, University of Liège). Copyright © 2011 John Wiley & Sons, Ltd.

1. INTRODUCTION

Within the diverse approaches that have been adopted in the last decades to model trabecular bone remodeling processes [1], some of them are qualified as phenomenological models. These are models whose goal is to predict the global mechanical behavior (displacement, strains, and

---

*Correspondence to: University of Liège, LTAS - Non Linear Computational Mechanics, Institute of Mechanics - Sart-Tilman Campus (B52) - B-4000 Liège. E-mail: mmengoni@ulg.ac.be
†Present address : Max Planck Institute for Polymer Research, Mainz, Germany

stresses) of a tissue or an organ, taking into account the microstructure, the applied loads, and the constraints imposed at the boundaries by the environment or the surrounding organs and tissues. Most of these models [2, 3, 4] compute the change of bone apparent density as a function of a given mechanical stimulus. Such a stimulus produces bone apposition or resorption in a way that the stimulus tends to a physiological level in the long-term (homeostasis). Some of these phenomenological models consider bone as an isotropic structural material, neglecting the role of the structural orientation in the remodeling process [5, 6, 7]. Others couple material density with orientation or anisotropy [8, 9, 10]. These phenomenological models are all built on constitutive material laws linking global stresses to global strains with internal variables representative of the evolving local microstructure. These models therefore need not only to be validated against remodeling data but the global constitutive law itself needs to be validated as well. The aim of this study is therefore to implement such a constitutive law and validate it.

The phenomenological approach to remodeling is used when modeling is performed at a macroscopic scale, typically the organ scale. To compensate for the lack of topological details, one needs to use accurate non-linear material properties at the continuum level for the underlying constitutive law. The use of such non-linear models based on morphological analysis has increased over the years [11, 12]. However, most studies using non-linear material models and/or large strains for bone remodeling propose models that are validated only against global remodeling pattern and not local bone mechanical behavior [13]. Other non-linear models validated against purely mechanical tests are usually not suitable for use in a finite strain framework [14, 15, 16]. For instance, Charlebois et al. [16] presented an anisotropic non-linear model accounting for plasticity and damage effects. Their model is based on a decomposition of the (Green-Lagrange) strain into elastic and plastic parts. However, while such a decomposition is subject to caution when a finite strain formulation is used, no details are given on how large rotations are handled for instance. These models also do not consider the possibility for the internal variables to evolve with the morphology. They can therefore not easily be used in remodeling situations. Other models describe the non-linear behavior of bone not as plasticity but as a bilinear elastic behavior, considering a reduction of the Young's modulus beyond a given strain level [17, 18, 19]. In particular, these bilinear elastic models do not allow for the accumulation of irreversible strains. Finally, one finds non-linear models for which the apparent parameters are extracted from linear FE analysis on the micro-structure [17, 18]. However, as pointed out by Christen et al. [20], geometrically non-linear (finite strains) analysis is to be used even when a micro-structure finite element approach to bone biomechanics is performed (as in [21]). Indeed non-linear geometric behavior due to large displacements/rotations such as buckling and bending of trabeculae has to be considered. However, until recently, mostly linear analysis was performed in finite element analysis on the micro-structure, mainly because of the computational cost associated to such non-linear models.

This work therefore presents a phenomenological, continuum-based, constitutive law that can be used in bone remodeling simulations in a finite strain framework. The constitutive law therefore aims at describing the non-linear mechanical behavior of trabecular bone in the range of small to moderate compressive strains. It considers an accumulation of plastic deformation and possible low softening due to early buckling of the microstructure. As on the local level the remodeling leads to a variation of the morphology, the phenomenological constitutive law is based on internal variables

representative of this morphology. These internal variables are included in the model in such a way that they can evolve according to a remodeling law.

2. NON-LINEAR CONTINUUM BASED MATERIAL MODEL.

The proposed constitutive model is built on a damage/repair remodeling model, first proposed by Doblaré and co-workers [10, 22]. This model has been chosen as a working base because it is one of the few models whose stimulus variation is justified through thermodynamical concepts of continuum mechanics. It is here enhanced to be coupled to an elastoplastic material behavior in a finite strains framework [23]. The presented constitutive law can therefore capture permanent strains of the tissue beyond the ones due to density variation. However, we present here only the purely mechanical part of the constitutive law, no variation due to remodeling is accounted for. In this section, second order tensors are in bold italic letters ($\boldsymbol{\sigma}$, $\boldsymbol{D}$ or $\boldsymbol{a}$), fourth order tensors in double line letters ($\mathbb{C}$ and $\mathbb{M}$), the dyadic product between two second order tensors is noted ":" ($\boldsymbol{a} : \boldsymbol{a} = a_{ij}a_{ij}$, summation over dummy indexes), the contraction product between a fourth order tensor and a second order one is noted ":" ($\boldsymbol{a} = \mathbb{C} : \boldsymbol{b}$ or $a_{ij} = C_{ijkl}b_{kl}$, summation over dummy indexes) and $\mathrm{tr}(\boldsymbol{a})$ and $\mathrm{dev}(\boldsymbol{a})$ are respectively the trace and the deviatoric parts of $\boldsymbol{a}$.

In finite strains, the current and initial configurations are significantly different. This implies that the expressions of variables, volume integrals etc. depend on the configuration, which is not the case under the small strains hypothesis. So, the use of a specific formulation is required to deal with finite strains. Especially, as constitutive laws must be invariant under changes of reference frame, they must be written in terms of objective quantities only (quantities that are frame independent). For an elastoplastic material in an hypoelastic formulation, the basic assumption consists in an additive decomposition of the strain rate (symmetric part of the spatial gradient of velocity), $\boldsymbol{D}$, into two parts : an elastic and reversible part, $\boldsymbol{D}^e$, and an irreversible plastic part, $\boldsymbol{D}^p$. Therefore stresses are represented by an evolution law of the type :

$$\overset{\triangledown}{\boldsymbol{\sigma}} = \overset{\triangledown}{\boldsymbol{\sigma}} \left(\boldsymbol{\sigma}, \boldsymbol{D}, \text{internal variables} \right) \tag{1}$$

where $\boldsymbol{\sigma}$ is the Cauchy stress tensor and $\overset{\triangledown}{\boldsymbol{\sigma}}$ is an objective derivative of the Cauchy stress tensor. The object of this section is to particularize this evolution law to the case of trabecular bone, keeping in mind it has to be used in remodeling situations. It therefore has to be built so that the internal variables depend on morphological parameters representing the bone apparent density and its anisotropy.

The bone tissue at a continuum level is considered as an anisotropic "organization" of elastoplastic trabeculae (local level). This "organization", as proposed in [10], is measured through a mean bone apparent density and its anisotropy uses the concept of fabric tensor as introduced in the work of Cowin [24]. The continuum damage framework is used not to capture actual damage at the local level, i.e. micro-cracks of the trabeculae, but to represent the bone macroscopic porosity and therefore measure the volume fraction. In terms of morphological data provided by computed tomography, damage is to be understood as a measure of the apparent density of the tissue ($\bar{\rho}$ or the bone volume fraction, BV/TV i.e. the bone volume over the total specimen volume). Its

anisotropy is measured by the fabric tensor (the fabric tensor $\hat{\boldsymbol{H}}$ is here normalized in such a way that $\mathrm{tr}(\hat{\boldsymbol{H}}) = 3$). The damage is therefore virtual and actually reflects the bone volume fraction and orientation that can evolve in remodeling situations. There is no actual damage in the tissue. The undamaged material is therefore the virtual situation of bone with zero porosity and perfect isotropy. It is the material considered at the trabecular tissue level, assumed to be linear elastic in [10, 22].

To use Doblaré and Garcia's model [10, 22] with bone trabeculae described with a material model other than linear elasticity, the effective stress definition in the representation of damage has to be chosen to enable a coupling of damage with non-linearities such as (visco-)plasticity. The main drawback of this model for coupling with plasticity is the use of a strain energy equivalence approach to represent the contribution of morphology. This continuum damage approach relates the stress level in the damaged material (Cauchy stress, $\boldsymbol{\sigma}$) with the stress in the undamaged material (effective stress, $\tilde{\boldsymbol{\sigma}}$) that leads to the same strain energy. Therefore, this damage approach looses the physical relation of damage to the surface density of defects. Keeping this physical relation would however allow the coupling of damage to plasticity by expressing the plastic criterion in terms of an effective stress tensor instead of the stress tensor. The plastic criterion would then be expressed for the undamaged material, here the trabecular material. Such a physical relation is kept using a strain equivalence approach to continuum damage instead of strain energy equivalence. This strain equivalence approach to continuum damage relates the stress level in the damaged material with the stress in the undamaged material (effective stress) that leads to the same strain. It gives an effective stress rate linked to the elastic strain rate by the generalized Hooke's law (in Equation (2), $\mathbb{C}^o$ is the elastic stiffness tensor, with parameters evaluated at the trabecular level) :

$$\overset{\triangledown}{\tilde{\boldsymbol{\sigma}}} = \mathbb{C}^o : (\boldsymbol{D} - \boldsymbol{D}^p) \tag{2}$$

The effective stress ($\tilde{\boldsymbol{\sigma}}$) is related through the Cauchy ($\boldsymbol{\sigma}$) stress by the use of a second order damage tensor, $\boldsymbol{d}$. It is formulated in a strain equivalence approach of damage so that it retrieves, when isotropic conditions are encountered, $d = 1 - E/E_0$, E being the Young's modulus of the bone tissue and E_0 the Young's modulus of the trabeculae. This damage tensor depends on morphological parameters ($\mathtt{BV/TV} : \bar{\rho}$ and fabric tensor : $\hat{\boldsymbol{H}}$) :

$$\boldsymbol{d} = \boldsymbol{I} - \bar{\rho}^{\beta} A \hat{\boldsymbol{H}} \tag{3}$$

In this definition (Equation 3), A is a calibration scalar parameter to retrieve the damage definition in isotropic conditions and β is defined so that the tissue Young's modulus is related to the density as : $E(\rho) \propto \rho^{\beta}$. The constitutive model (Equation 2) defines an effective stress, $\tilde{\boldsymbol{\sigma}}$, acting on the effective area of the material. The Cauchy stress ($\boldsymbol{\sigma} = \boldsymbol{s} + p\boldsymbol{I}$) is obtained by taking into consideration the effect of the structural morphology represented by the damage tensor. According to Lemaitre and Desmorat [25, 26], one of the only effective stress definition for anisotropic damage that fulfills the conditions of being symmetric, independent of the strain behavior, compatible with the thermodynamics (existence of a stress potential and a principle of strain equivalence), and that can express different effects of damage on the hydrostatic behavior and deviatoric part of stress (by

means of a scalar parameter, η), is represented by :

$$\tilde{\boldsymbol{\sigma}} = \mathrm{dev}(\boldsymbol{H s H}) + \frac{p}{1 - \frac{\eta}{3}\mathrm{tr}(\boldsymbol{d})}\boldsymbol{I} \tag{4}$$

In this definition of effective stress (Equation 4), the second-order tensor $\boldsymbol{H}$ is introduced to simplify the notation : $\boldsymbol{H} = (\boldsymbol{I} - \boldsymbol{d})^{-1/2}$ (such a tensor is well defined being the positive square root of the inverse of the positive definite symmetric tensor $\boldsymbol{I} - \boldsymbol{d}$). This equation thus gives, if an isotropic fabric tensor were considered : $\tilde{\boldsymbol{\sigma}} = \boldsymbol{\sigma}/(1 - d)$. In order to keep a linear relation between effective and Cauchy stress, one can write

$$\tilde{\boldsymbol{\sigma}} = \mathbb{M} : \boldsymbol{\sigma} \tag{5}$$

where $\mathbb{M}$ is a fourth order symmetric tensor defined from $\boldsymbol{H}$ as (summation over dummy indexes) :

$$M_{ijkl} = H_{ik}H_{jl} - \frac{1}{3}(H_{in}H_{nj}\delta_{kl} + H_{kn}H_{nl}\delta_{ij}) + \frac{1}{9}H_{nm}H_{mn}\delta_{ij}\delta_{kl} + \frac{1}{3}\frac{1}{1 - \frac{\eta}{3}d_{nn}}\delta_{ij}\delta_{kl} \tag{6}$$

The plastic part of the strain rate $\boldsymbol{D}^p$ can be calculated through the normality rule applied to the plastic criterion (associated plasticity) expressed in term of the effective stress. This plastic criterion is therefore the plastic criterion for the undamaged material. It is here the criterion for a single trabeculae mechanical behavior which is assumed to be pressure independent. Therefore, a simple von Mises criterion is chosen with only isotropic hardening allowed, giving a plastic strain rate as :

$$\boldsymbol{D}^p = \frac{3}{2}\frac{\overset{\bullet}{\lambda}}{\tilde{\sigma}_{eq}}\mathrm{dev}(\boldsymbol{H\tilde{s}H}) \tag{7}$$

where $\overset{\bullet}{\lambda}$ is the plastic multiplier and $\tilde{\sigma}_{eq}$ is the equivalent stress used for the von Mises criterion :

$$\tilde{\sigma}_{eq} = \sqrt{\frac{3}{2}\tilde{\boldsymbol{s}} : \tilde{\boldsymbol{s}}} \tag{8}$$

The constitutive law is integrated in a finite element framework according to an iterative staggered scheme (adapted from the isotropic damage integration proposed in [23, 27]). It is implemented in Metafor [28], an in-house object-oriented finite element code, using the following set of equations, whose details have been presented in this paper :

$$
\begin{aligned}
\text{initial damage tensor :} \quad & \boldsymbol{d}, \text{ computed from morphological analysis (Equation 3)} \\
\text{structural tensor :} \quad & \boldsymbol{H} = (\boldsymbol{I} - \boldsymbol{d})^{-1/2} \\
\text{effective stress :} \quad & \tilde{\boldsymbol{\sigma}} = \mathrm{dev}(\boldsymbol{H s H}) + \frac{p}{1 - \frac{\eta}{3}\mathrm{tr}(\boldsymbol{d})}\boldsymbol{I} \\
\text{strain rate :} \quad & \boldsymbol{D} = \boldsymbol{D}^e + \boldsymbol{D}^p \\
\text{constitutive law :} \quad & \overset{\triangledown}{\boldsymbol{\sigma}} = \mathbb{C}^o : (\boldsymbol{D} - \boldsymbol{D}^p)
\end{aligned}
$$

The time-step integration can be succinctly described as follows : starting from a known stress state ($\boldsymbol{s}$, p) and damage ($\boldsymbol{d}$), an elastic predictor of the effective stress is computed. If needed, a plastic

correction is performed at constant damage thanks to a radial-return process (read [29] for details on the plasticity computation), giving plastic deformations and final effective stress. When remodeling is considered, damage evolution is computed and a new value of the damage tensor is determined. Stresses and plastic strains are then re-evaluated, up to convergence of the updated damage tensor norm. The Cauchy stress is finally computed from the effective stress and the new damage tensor. The final morphological data due to remodeling can be extracted from the obtained damage tensor.

3. MATERIAL AND METHODS

Under compressive load, the mechanical behavior of trabecular bone exhibits characteristics of an elastoplastic cellular solid. Such elastoplastic cellular materials [30, 31] present a behavior in compression showing a decrease of the apparent tangent stiffness before reaching a maximal force. Beyond apparent engineering strains at maximal force, smooth and gradual softening occurs until a plateau is reached. It is followed, before the occurrence of failure, by a final apparent hardening due to collapse of the cells. The proposed continuum based mechanical behavior should therefore be validated against experimental data obtained for mechanical tests of trabecular bone as well as materials with bone-like microstructure undergoing small to moderate strains. As the constitutive law is to be used eventually in remodeling problems for which apparent strains are limited, the proposed law has to be validated up to the reaching of the plateau.

The presented continuum-based formulation was applied to three different materials : two engineered cellular solid materials showing bone-like microstructure, aluminum and Polylactic acid foams (Figure 1 shows 3D visualization of one of the tested aluminum foam samples), and cancellous bone tissue of a deer antler.

For each type of material, cylindrical specimens were used. Images of the microstructure were acquired using a X-Ray micro-tomography imaging system (μCT). For each specimen, the following structural parameters were determined from the μCT data (software CT-Analyser, Skyscan, Belgium) : bone volume fraction (BV/TV), the eigenvalues ($E1$, $E2$, $E3$) and eigenvectors (E-vectors 1 to 3) of the Mean Intercept Length (MIL) tensor, and the degree of anisotropy (DA), which is the ratio of the max eigenvalue to the min one. The MIL tensor is related to the stereological measurement of the microstructural arrangement. Cowin [8] defined a fabric tensor $\hat{H}$ related to the MIL tensor M by $\hat{H} = M^{-1/2}$. Such a tensor is well defined being the positive square root of the inverse of the positive definite symmetric tensor M. This definition of the fabric tensor is the one used here. The samples were then compressed along their main axis in a mechanical testing device and load-displacement data were acquired.

The first material that has been tested is fabricated from highly porous aluminum alloys. The Duocel aluminum foam (ERG, Oakland, CA) from which the samples were extracted is composed of 6101 T6 aluminum alloy. Fifteen specimens were used (diameters and heights of respectively about 8 and 16 mm), five of which will be referred as "dense" (mean bone volume fraction over the five samples $\bar{\rho} = 12.8\%$), five have a "middle" density ($\bar{\rho} = 7.3\%$), and the last five have a "low" density ($\bar{\rho} = 4.4\%$). Images were generated using a X-Ray micro-tomography imaging system (μCT 20, Scanco Medical, Switzerland), a compact fan-beam type tomograph [32], also referred to as a desktop μCT, at a $34 \times 34 \times 34$ μm^3 resolution. The samples were compressed
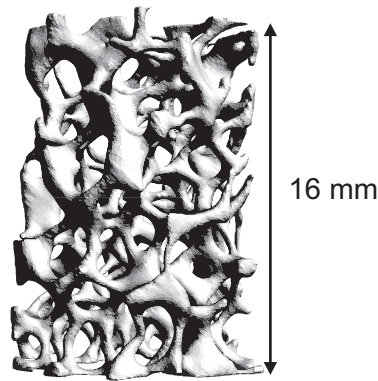
Figure 1. 3D visualization of a specimen of aluminum foam obtained from μCT images.

Table I. Material parameters at the local level

Material	Young's modulus [GPa]	Poisson's ratio [−]	Yield stress [MPa]	Hardening parameter [MPa]
Duocel Foam	69.0	.33	200.0	200.0
PLA	3.2	.33	75.0	0
Deer antler	8.1	.33	95.0	820.0

in a stepwise fashion from 0% to 16% apparent engineering strain (mechanical testing and μCT acquisition are detailed by Nazarian and Müller in [32]). The material parameters used to describe the local level (the "trabecular" mechanical behavior) were chosen from the literature on this specific alloy [33, 34, 35, 36] and are reported in table I. We assumed a low linear isotropic hardening ($h = 200\ MPa$, leading to a tangent modulus of $E_t = 200.5\ MPa$).

The second material is a foam composed of Polylactic acid (PLA) and an amphiphilic block copolymer of lactide and ethylene oxide (PEO), prepared by the CERM, University of Liège [37]. PLA is a biocompatible, biodegradable, and easy processable polymer and has therefore received considerable attention for the manufacturing of three-dimensional polymer scaffolds. Their properties can be easily tuned, for example the wettability can be increased by adding a hydrophilic copolymer. The freeze-drying technique allows the preparation of PLA foam with highly organized longitudinal and random pores. Mixtures of PDLLA (Purac, $Mn = 136000\ g/mol$) and PEO-b-PDLLA [$Mn(PEO) = 5000\ g/mol$; $Mn(PDLLA) = 17700\ g/mol$] were prepared as follows : the (co)polymers were dissolved in dimethylcarbonate at a concentration of $3\ wt : vol\%$ with a proportion of $5\ wt\%$ of PEO in respect to the whole polymer mass. The solution was frozen for one night at $-70\ ^oC$, dried by vacuum sublimation for $48\ h$ at $-10\ ^oC$, followed by a $48\ h$ period at $0\ ^oC$, and finally at room temperature until it reached a constant weight. A single specimen was used (8.2 mm in diameter and 12.5 mm in height, with an apparent volume density of 15%). Tomographic images of the sample were generated using a μCT imaging system (Skyscan 1172, Skyscan, Belgium), a compact closed cone-beam type desktop tomograph, at a $8.64 \times 8.64 \times 86.4\ \mu m^3$ resolution. It was compressed from 0% to 42% apparent engineering strain. Only a few studies have investigated the mechanical behavior of PLA as in most applications PLA is reinforced by fibers [38, 39, 40]. However, the elastic behavior of the PLA is usually assumed linear. The plasticity is here assumed to be a von Mises perfectly plastic behavior. The yield stress has been chosen to fit
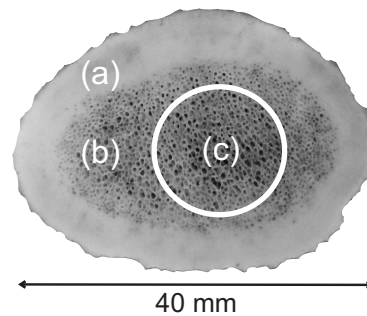
Figure 2. Transverse view of a deer antler : (a) compact bone - (b) cancellous bone - (c) extraction site.

the experimental results. The set of material parameters used to describe the local level is reported in table I.

The last material presented is cancellous tissue of a deer (*Cervus Elaphus*) antler, prepared at the Department of Clinical Sciences, Faculty of Veterinary Medicine, University of Liège [41, 42]. The antlers of cervids are constituted of bone tissue covered with velvet in the early stage of growth. This bone tissue is composed of a central core of cancellous bone surrounded by a thick outer layer of compact bone (Figure 2). The core cancellous bone presents a cellular structure. It is the part used here. A single deer antler specimen was used in this work (7.8 mm in diameter and 11.96 mm in height, with an apparent volume density of 18.7%). It was collected before antler casting, during the active growth phase when the antler is still covered by velvet. The sample, made of primary bone tissue, was machined from the core of the antler main beam [41]. Tomographic images were taken using the same tomograph used for the previous material. It was compressed from 0% to only 4.1% apparent engineering strain. As for the the PLA, only few studies have investigated the mechanical properties of the cancellous part of deer antler [43] while the cortical part has been widely investigated ([44, 45, 46] among many more). One of the reasons to this difference is the difficulty of isolating the cancellous core of the antler as it is very brittle. The yield properties of the trabeculae are here assumed to be equivalent to the one calculated in [44] for cortical bone as the Young's modulus in [44] is similar to the Young's modulus reported in [43] for cancellous bone. The set of material parameters used to describe the local level is reported in table I.

All the specimens described were modeled as cylinders of appropriate dimensions. They were meshed with 3136 elements (hexahedral 8-nodes elements with selective reduced integration) i.e. 16 layers of 196 elements (Figure 3). The morphology of each specimen was described through the use of the damage tensor. This tensor was computed (Equation 3) using morphology data (BV/TV, fabric tensor) extracted from the structural analysis on the μCT images of the corresponding tested specimen. For each specimen, this damage tensor and the other material parameters (table I) were assigned to each element of the FE mesh. To represent the experimental boundary conditions, a displacement was applied on one side of the cylinder (vertical displacement with free in plane movement) while the other side of the cylinder was modeled to be in contact (frictionless conditions) with a rigid plane. On the contact plane, one central node of the cylinder was constrained in the horizontal plane to prevent rigid body modes. The displacement was applied so that it leaded to a 10% (Duocel foam), 20% (PLA foam) or 4% (deer antler) apparent compressive engineering strain. The apparent strain levels achieved justify the use of a finite strains formalism for the finite
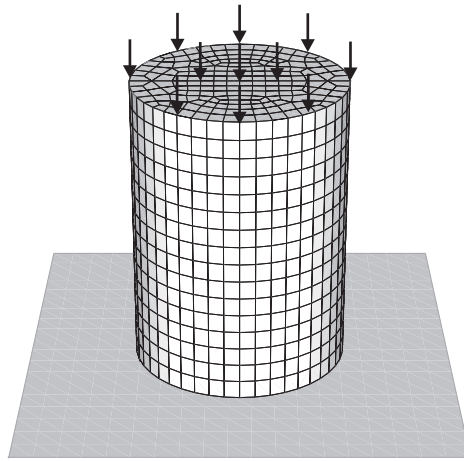
Figure 3. Hexahedral mesh of the homogeneous cylinder model of a specimen with its boundary conditions.

Table II. Morphological parameters extracted from the CT images analysis (mean ($\pm$ std) for the Duocel foam samples)

Material	BV/TV [%]	DA [$-$]
Duocel Foam (high density)	12.800 (1.007)	1.059 (0.009)
Duocel Foam (middle density)	7.262 (0.502)	1.084 (0.013)
Duocel Foam (low density)	4.431 (0.276)	1.137 (0.033)
PLA	14.5	2.144
Deer antler	8.53	2.583

element computation. FE analyses were performed to compute the external force needed to apply the displacement for each sample. It was then compared to the experimental one. We finally also compared the results obtained with the presented anisotropic elastoplastic model to materials models accounting only for anisotropic elasticity or only for elastoplasticity. The anisotropic elasticity model was achieved by setting to zero Equation (7). The isotropic elastoplasticity model needed an isotropic damage variable accounting only for BV/TV. This was achieved by setting the fabric tensor to the unit tensor instead using of a structural fabric to compute the damage tensor.

The morphological analysis software CT-Analyser allows for a definition of a region of interested (ROI) to extract the morphological data. Initially, the morphological data were extracted over the whole volume of the specimens (Table II). The ROI was therefore set for each specimen as one cylinder over the whole volume. Later, the impact of the volume on which the morphological data were extracted was analyzed. Each cylinder was virtually divided into 4 or 8 cylinders, each of one quarter or one eighth of the full height. The morphological data were then extracted on each of these ROIs. Instead of one damage tensor for the whole specimen, the FE model therefore presents 4 or 8 damage tensors, each assigned to the corresponding finite elements in the discretization.

4. RESULTS AND DISCUSSION

Although all the samples used are cellular materials, they present, within their testing range, different types of behaviors in compression (Figure 4) : Duocel foams (Figure 4(a)) exhibit a
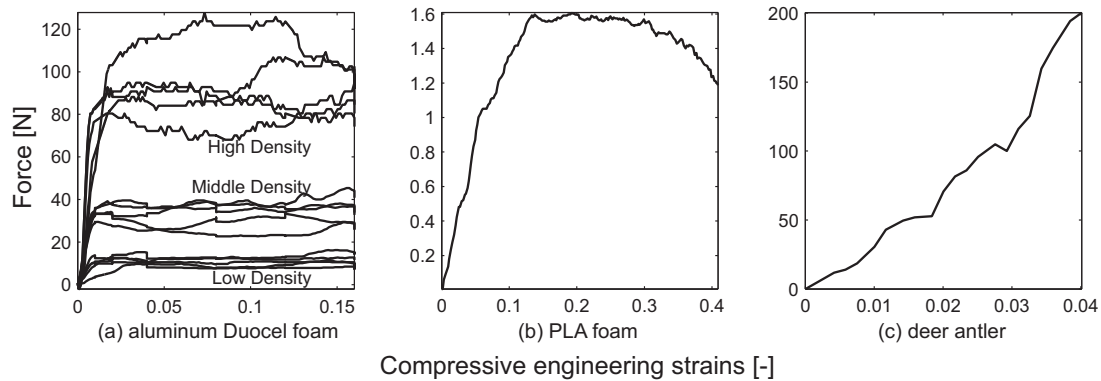
Figure 4. Experimental forces vs. compressive engineering strains for the three types of material presented.

mechanical behavior typical of cellular solids as described earlier. Specially, the experimental force presents a characteristic plateau for the lower and middle density samples. Figure 4(a) also demonstrates the dependence of the mechanical apparent behavior on the apparent density. Lower density samples exhibit lower apparent stiffness in the linear part of the force-displacement curves and their maximal forces are lower than for higher densities samples. However, within the testing range, none of the low density and middle density samples seems to present final hardening. The PLA sample (Figure 4(b)) is tested only up to the appearance of softening after reaching the maximal force, the force plateau is not present in the experimental data. Both the Duocel foam and PLA foam material exhibit within their testing range an apparent yielding behavior. Regarding the deer antler cancellous tissue specimen (Figure 4(c)), only the initial increase of tangent stiffness is present as the sample is tested only to a low strains level. The maximal displacement tested seems to be lower than the one needed to reach the maximal force.

Figures 5 to 9 present the results of the FE analyses in term of a comparison between the computed force and the experimental one for the corresponding sample. For the Duocel foam samples, the results for each set of density level are presented as a mean (and standard deviation) over the set for the relative difference between the computed force and the experimental one (Figures 5(a) to 7(a)). Detailed results for an arbitrary sample are also presented (Figures 5(b) to 7(b)).

The results are first analyzed for morphological data extracted over the whole volume of the specimens. This case is referred to as "1 ROI" in the corresponding figures.

The predicted force-engineering strain behavior for both the Duocel samples (Figures 5 to 7) and the PLA foam sample (Figure 8) present the same overall behavior as the experimental one in the range of strains considered here. We can retrieve the apparent linear behavior as well as the maximal force. This maximal force is represented with an error of less than 10% for the high density Duocel samples (Figure 5(a)) and of about 11% for the middle density ones (Figure 6(a)). Moreover, the low density Duocel samples show an error on the maximal force (achieved for all samples at about 3% of compression - Figure 4(a)) of only 2.5%. Finally, this maximal force is computed with an error of less than 0.5% for the PLA foam (Figure 8). However, one has to keep in mind that the yield limit for this sample was chosen to fit the experimental results, having such a small error was thus expected. The transition between the linear part of the curves and the reach of maximal force is however ill represented. Indeed, the appearance of yield shows an difference

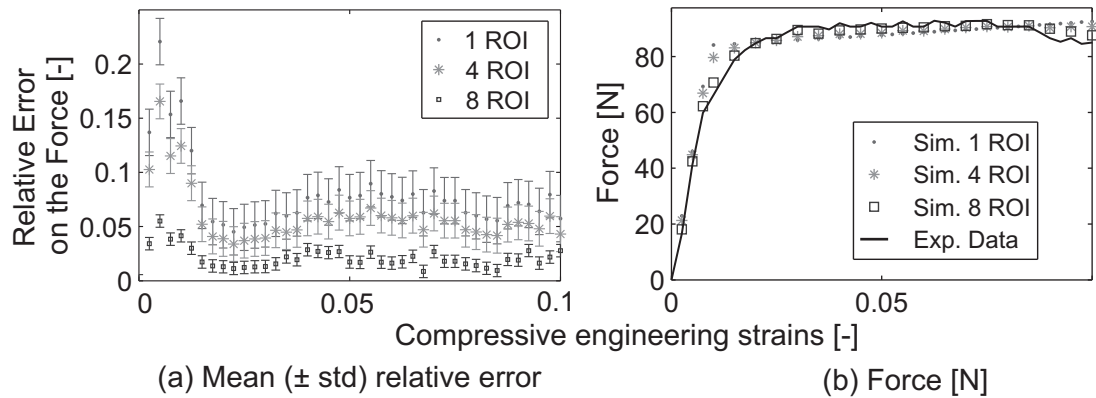(a) Mean (± std) relative error   (b) Force [N]

Figure 5. Dense Duocel Foam Samples : computed (Sim.) and experimental forces [N] vs. compressive engineering strains [-]. (a) relative error on the force - mean and std., (b) force for an arbitrary sample
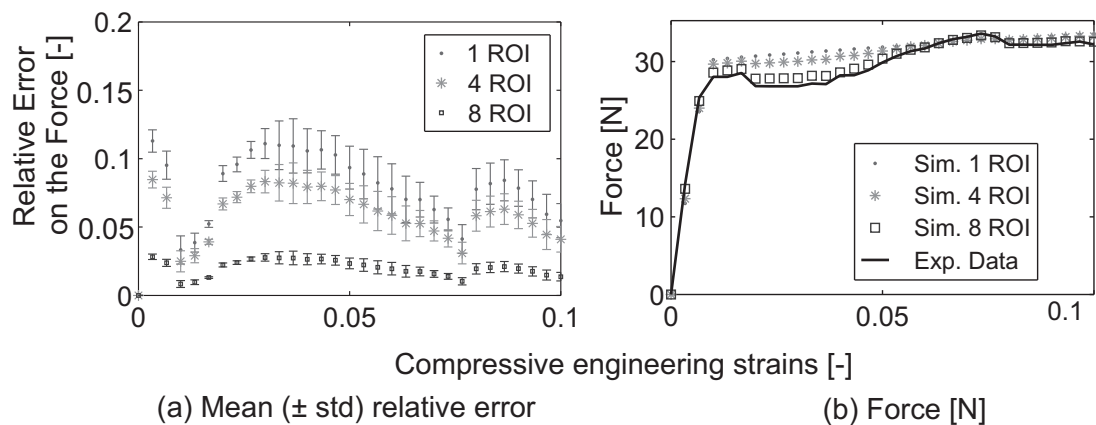

(a) Mean (± std) relative error   (b) Force [N]

Figure 6. Middle Density Duocel Foam Samples : computed (Sim.) and experimental forces vs. compressive engineering strains (a) relative error on the force - mean and std., (b) force for an arbitrary sample.

up to more than 1% of engineering strain for the high density Duocel samples (Figure 5) or the PLA foam (Figure 8). For the Duocel samples (Figures 5 to 7), the only material reaching the plateau in the experimental data, the softening occurring before reaching the plateau cannot be represented with this morphology data. Indeed, the computed force tends to increase almost linearly after reaching the maximal force. Therefore, the error on this force increases as well. Specially, the abrupt decrease of the experimental force such as present in the low density Duocel samples at about 4% of engineering strains (Figure 4(a)) cannot be represented by the model. The error on the computed force increases in these conditions from 2.5% to 15% (Figure 7). Concerning the deer antler sample (Figure 9), only the mean stiffness over the computed strain range can be represented. The use of structural parameters averaged over the entire volume seems therefore not appropriate to represent the non-linear behavior of the force for all materials. It should be noticed however that for the PLA foam and deer antler, as only one specimen was used, the presented results (both experimental and computational) may not be representative.

A closer analysis of the μCT images (such as the 3D visualization on Figure 1) shows that the repartition of the density and its orientation is not homogeneous on the specimens. Therefore, the choice to compute one set of morphological parameters to represent the whole specimen is not
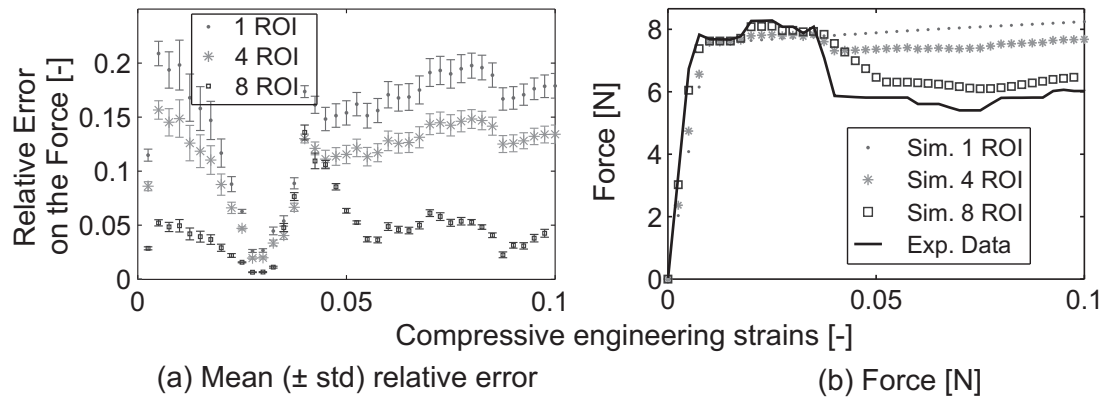
Figure 7. Low Density Duocel Foam Samples : computed (Sim.) and experimental forces vs. compressive engineering strains (a) relative error on the force - mean and std., (b) force for an arbitrary sample.
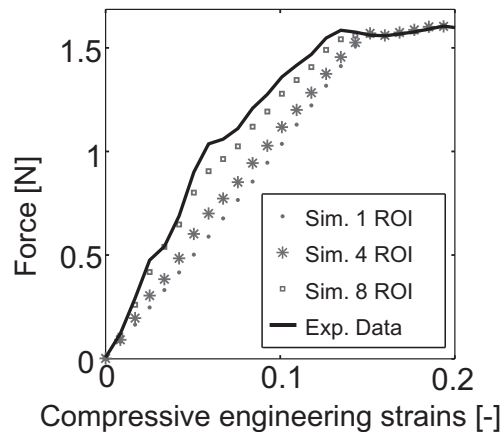

Figure 8. PLA Sample : computed (Sim.) and experimental forces vs. compressive engineering strains.

representative of the actual specimen structure. The same morphological parameters were then extracted for each cylinder on smaller regions of interest. This therefore allows for the representation of force variations due to more local behavior. Extracting the material parameters over 4 ROIs (referred to as "4 ROI" in Figures 5 to 9) already reduces the error observed on the linear part of the force by about 20%. It also allows a better computation of early softening for which the error is reduced by about 4% (Figure 7(b)). When computing the force with material parameters extracted over 8 ROIs (referred to as "8 ROI" in Figures 5 to 9), the predicted force can fit details of the experimental force variations on the non-linear part of the curve. The relative error on the force is reduced for all samples below 5% over the computed strain range except when the experimental force shows abrupt variations such as the abrupt reduction of force before reaching the plateau (Figure 7(a) and (b)). For both the PLA foam and the deer antler sample, reducing the size of the ROI allows to better fit the curvature of the almost linear part of the force (Figures 8 and 9), reducing the maximal error from 40% to less than 10% for the PLA foam and from 100% to 15% for the deer antler. We therefore seem to get a convergence of the computed force to the experimental one using small ROIs. However, this convergence is achieved at the expense of the computational cost.
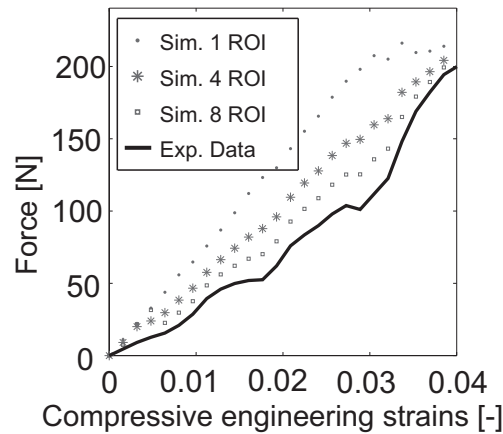
Figure 9. Deer antler Sample : computed (Sim.) and experimental forces vs. compressive engineering strains.

Even though the Duocel foam samples all have a low degree of anisotropy (Table II), the use of an anisotropic material accounting for the fabric directions, instead of an isotropic one accounting only for BV/TV (Figure 10), allows to better capture not only the apparent stiffness of the sample but also the apparent yield stress and the engineering strain at which apparent yield is achieved. The use of an isotropic model for the Duocel foams in applications where the maximal force is of importance would conclude to an overestimation of about 11% on the force for both the high density and the middle density samples (Figures 10(a) and (b)). For the low density samples, the use of an isotropic model would lead to an accurate estimation of the maximal force at the correct strain level but the post-yield behavior is ill-represented, leading to errors up to 30% (Figure 10(c)).

The importance of using an elastoplastic model for the Duocel samples is also outlined in Figure 10(a) to (d). It can be seen that an elastic material can account only, as can be expected of such a linear behavior, for the initial stiffness of the samples. The use of an elastic anisotropic material would here lead to assume a slight increase of the tangent stiffness instead of a decrease before yield. This lead, for the maximal simulated strain, to an error on the force of more than 1000% for some samples. The introduction of elastoplasticity for this material is therefore even more essential than the use of an anisotropic material.

Concerning the PLA foam sample, Figure 11(a) shows the importance of using a non-linear material model. Indeed, the force computed with an elastic material model continue to increase monotonously after reaching the experimental yield limit. This lead, for the maximal simulated strain, to an error on the force of about 300%. In this case, the use of an anisotropic model, while the degree of anisotropy is higher than for the Duocel foams (Table II), is less determinant than the use of a non-linear one. The error on the computed force at the end of loading is indeed of only 6% with an isotropic elastoplastic model. This would allow to conclude, on this particular sample for the given test conditions, that the non-linearity of the material has more impact on its response to load than its anisotropic structure.

The deer antler sample however shows almost no difference on the force computed with an elastic or an elastoplastic material model when the anisotropy is considered (Figure 11(b)). This can be explained as the maximal strain achieved in this compression test is small (only 4% of engineering strain), the elastic model therefore seems to be sufficient to describe the antler mechanical behavior.
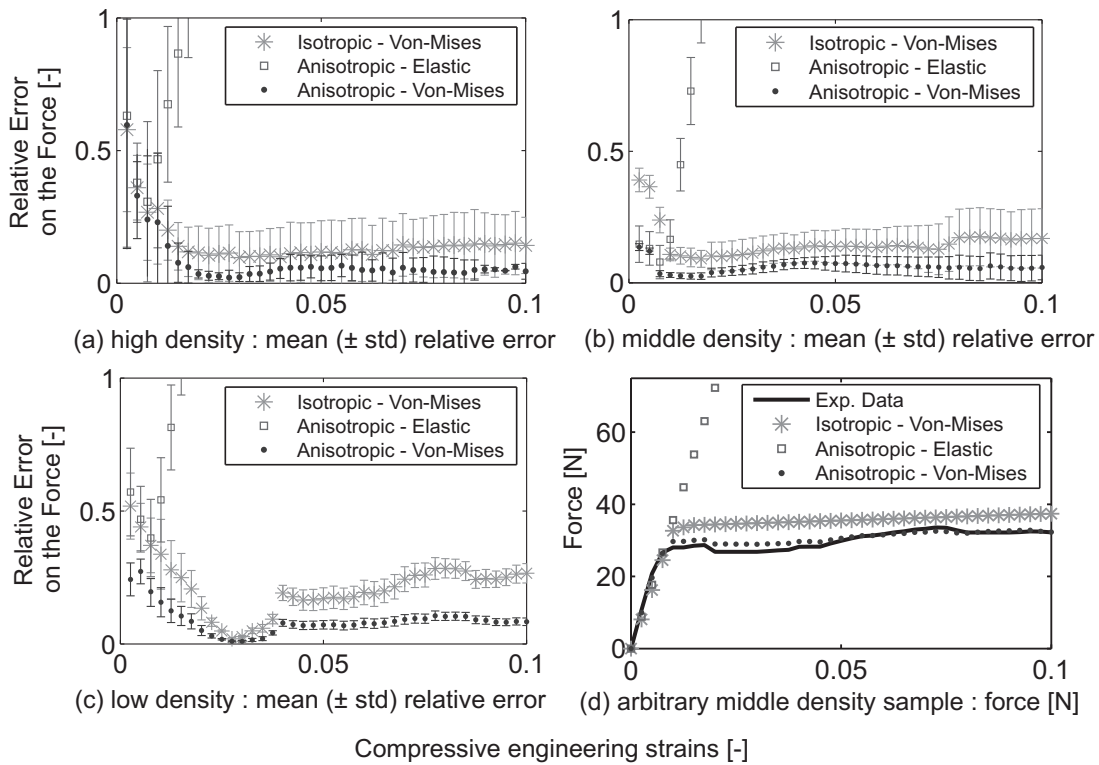
Figure 10. Comparison of the force vs. compressive engineering strains for three different material models (Duocel foam samples, 8 ROI) : anisotropic elastoplastic (von Mises) material - material model presented in this study ; isotropic elastoplastic (von Mises) material ; anisotropic elastic material
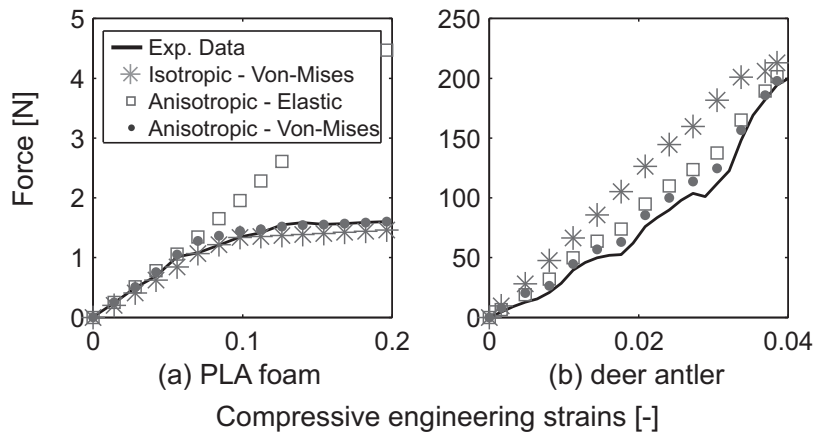

Figure 11. Comparison of the force vs. compressive engineering strains for three different material models (PLA foam and deer antler, 8 ROI) : anisotropic elastoplastic (von Mises) material - material model presented in this study ; isotropic elastoplastic (von Mises) material ; anisotropic elastic material

However, the use of an isotropic model for the deer antler leads to errors on the computed force of about 30% throughout most of the strain range. This would therefore allow to conclude, on this particular sample for the given test conditions, that the anisotropic structure of the material has more impact on its response to load than its non-linearity.

5. CONCLUSIONS

In the present work, a phenomenological constitutive law based on morphological data acquisition is detailed. It provides a non-linear material model of the mechanical response of bone-like materials, accounting for early post-yield behavior of the structure. This constitutive model has been successfully applied to three materials presenting bone-like morphology undergoing moderate monotonic compression.

We showed that, for the presented materials and test conditions, the representation of the morphology through `BV/TV` and the fabric tensor are required to capture the apparent yield stress and strains even for low degrees of anisotropy. The introduction of a non-linearity such as elastoplasticity is essential to the understanding of the mechanical behavior in compression for strains beyond the yield limit. However, for applications where the strains are limited, the use of an elastic anisotropic model is sufficient to represent the force accurately. Using this model for morphological data extracted for regions of interests (ROI) small enough, we showed that one can retrieve not only the linear behavior of the structure but also the non-linear behavior such as the apparent yield stress and strain and early post yield softening. Using ROIs one eighth of the total volume of the specimens, we reduced the relative error on the force below 5% over the computed strain range except when abrupt variations of the force are observed. While the state-of-the-art in the use of material parameters extracted from the morphology is to assign different material parameters to each finite element [11, 14, 19, 47, 48], the presented results show that the computation of the maximal force as well as some non-linear measures (yield stress and strain for instance) can be achieved without the need to consider very small ROIs. The determination of the optimal size of these ROIs should consider several parameters such as the degree of local behavior needed in the macroscopic model but also the discretization (and therefore computation) cost. This type of global mechanical models is indeed presented as a possible solution for computationally costly models such as micro finite elements. The integration of more local behavior should therefore not lead to an excessive increase of the computation cost.

While the application of this material model seems to be valid for the presented materials in compression, it still has to proof itself on other materials, specially using more samples of bone and not mainly bone-like materials. Furthermore, for material for which the local non-linear behavior is not well known (here the PLA foam and the deer antler), loading/unloading tests should be carried out to ensure the non-linear behavior is indeed an irreversible (plastic-like) behavior and not another type of non-linearity (non-linear elasticity, micro-cracks leading to damage, ...). Finally, the model should also be tested on other mechanical tests such as traction or bending.

Prepared using cnmauth.cls

REFERENCES

1. Cowin SC, Hegedus DH. Bone remodeling i: theory of adaptive elasticity. *Journal of Elasticity* Jul 1976; **V6**(3):313–326, doi:10.1115/1.3138584.

2. Cowin SC. Tissue growth and remodeling. *Annu Rev Biomed Eng* 2004; **6**:77–107, doi: 10.1146/annurev.bioeng.6.040803.140250.

3. Roberts WE, Huja S, Roberts JA. Bone modeling: biomechanics, molecular mechanisms, and clinical perspectives. Seminars in Orthodontics 2004, doi:10.1053/sodo.2000.8083. Volume 10, Issue 2, June 2004, Pages 123-161.

4. Beaupré GS, Orr TE, Carter DR. An approach for time-dependent bone modeling and remodeling-application: a preliminary remodeling simulation. *Journal of Orthopedic Research* Sep 1990; **8**(5):662–670, doi: 10.1002/jor.1100080507.

5. Carter D, Orr T, Fyhrie D. Relationships between loading history and femoral cancellous bone architecture. *Journal of Biomechanics* 1989; **22**(3):231 – 244, doi:10.1016/0021-9290(89)90091-2.

6. Huiskes R, Weinans H, Grootenboer H, Dalstra M, Fudala B, Slooff T. Adaptive bone-remodeling theory applied to prosthetic-design analysis. *Journal of Biomechanics* 1987; **20**(11-12):1135 – 1150, doi:10.1016/0021-9290(87)90030-3.

7. Beaupré GS, Orr TE, Carter DR. An approach for time-dependent bone modeling and remodeling–theoretical development. *Journal of Orthopedic Research* Sep 1990; **8**(5):651–661, doi:DOI: 10.1002/jor.1100080506.

8. Cowin SC. Wolffs law of trabecular architecture at remodelling equilibrium. *Journal of Biomechanical Engineering* 1986; **108**:83–88, doi:10.1115/1.3138584.

9. Jacobs CR, Simo JC, Beaupre GS, Carter DR. Adaptive bone remodeling incorporating simultaneous density and anisotropy considerations. *Journal of Biomechanics* Jun 1997; **30**(6):603–613, doi:10.1016/S0021-9290(96)00189-3.

10. Doblaré M, García JM. Anisotropic bone remodelling model based on a continuum damage-repair theory. *Journal of Biomechanics* Jan 2002; **35**(1):1–17, doi:10.1016/S0021-9290(01)00178-6.

11. Keyak JH. Improved prediction of proximal femoral fracture load using nonlinear finite element models. *Medical Engineering & Physics* 2001; **23**(3):165 – 173, doi:10.1016/S1350-4533(01)00045-5.

12. Chevalier Y, Pahr D, Zysset PK. The role of cortical shell and trabecular fabric in finite element analysis of the human vertebral body. *Journal of Biomechanical Engineering* 2009; **131**(11):1110 031 – 11100 312, doi: 10.115/1.3212097.

13. Besdo S. Determination of dynamically adapting anisotropic material properties of bone under cyclic loading. *Journal of Biomechanics* Jan 2011; **44**(2):272–276, doi:10.1016/j.jbiomech.2010.10.005.

14. Gupta A, Bayraktar HH, Fox JC, Keaveny TM, Papadopoulos P. Constitutive modeling and algorithmic implementation of a plasticity-like model for trabecular bone structures. *Computational Mechanics* 2007; **40**(1):61 – 72, doi:10.1007/s00466-006-0082-5.

15. Garcia D, Zysset PK, Charlebois M, Curnier A. A three-dimensional elastic plastic damage constitutive law for bone tissue. *Biomechanics and Modeling in Mechanobiology* 2009; **8**(2):149–165, doi:10.1007/s10237-008-0125-2.

16. Charlebois M, Jirásek M, Zysset P. A nonlocal constitutive model for trabecular bone softening in compression. *Biomechanics and Modeling in Mechanobiology* 2010; **9**:597–611, doi:10.1007/s10237-010-0200-3.

17. Niebur GL, Feldstein MJ, Yuen JC, Chen TJ, Keaveny TM. High-resolution finite element models with tissue strength asymmetry accurately predict failure of trabecular bone. *Journal of Biomechanics* 2000; **33**(12):1575 – 1583, doi:10.1016/S0021-9290(00)00149-4.

18. Bayraktar HH, Morgan EF, Niebur GL, Morris GE, Wong EK, Keaveny TM. Comparison of the elastic and yield properties of human femoral trabecular and cortical bone tissue. *Journal of Biomechanics* 2004; **37**(1):27 – 35, doi:10.1016/S0021-9290(03)00257-4.

19. Bessho M, Ohnishi I, Matsumoto T, Ohashi S, Matsuyama J, Tobita K, Kaneko M, Nakamura K. Prediction of proximal femur strength using a ct-based nonlinear finite element method: Differences in predicted fracture load and site with changing load and boundary conditions. *Bone* 2009; **45**(2):226 – 231, doi:10.1016/j.bone.2009.04.241.

20. Christen D, Webster D, Müller R. Multiscale modelling and nonlinear finite element analysis as clinical tools for the assessment of fracture risk. *Philosophical Transactions of The Royal Society A* 2010; **368**(1920):2653–2668, doi:10.1098/rsta.2010.0041.

21. Verhulp E, van Rietbergen B, Müller R, Huiskes R. Indirect determination of trabecular bone effective tissue failure properties using micro-finite element simulations. *Journal of Biomechanics* 2008; **41**(7):1479 – 1485, doi: 10.1016/j.jbiomech.2008.02.032.

22. García JM, Doblaré M, Cegonino J. Bone remodelling simulation: a tool for implant design. *Computational Materials Science* Sep 2002; **25**(1-2):100–114, doi:10.1016/S0927-0256(02)00254-9.

23. Mengoni M, Ponthot JP. Isotropic continuum damage/repair model for alveolar bone remodeling. *Journal of Computational and Applied Mathematics* 2010; **234**:2036–2045, doi:10.1016/j.cam.2009.08.061.

24. Cowin SC, Hart RT, Balser JR, Kohn DH. Functional adaptation in long bones: establishing in vivo values for surface remodeling rate coefficients. *Journal of Biomechanics* 1985; **18**(9):665–684, doi:10.1016/0021-9290(85)90022-3.

25. Lemaitre J, Desmorat R. *Engineering Damage Mechanics: Ductile, Creep, Fatigue and Brittle Failures*. Springer, 2005.

26. Desmorat R, Otin S. Cross-identification isotropic/anisotropic damage and application to anisothermal structural failure. *Engineering Fracture Mechanics* 2008; **75**:3446–3463, doi:10.1016/j.engfracmech.2007.05.011.

27. Jeunechamps PP. Simulation numérique, à l'aide d'algorithmes thermomécaniques implicites, de matériaux endommageables pouvant subir de grandes vitesses de déformation. Application aux structures aéronautiques soumises à impact. Phd thesis (in French), University of Liège (Belgium), School of Engineering, Aerospace and Mechanics Department, 2008.

28. Metafor. *A large strain finite element code*. LTAS - MN2L - University of Liège, http://metafor.ltas.ulg.ac.be/ 2011.

29. Ponthot JP. Unified stress update algorithms for the numerical simulation of large deformation elasto-plastic and elasto-viscoplastic processes. *International Journal of Plasticity* 2002; **18**:91–126, doi:10.1016/S0749-6419(00)00097-8.

30. Gibson I, Ashby M. *Cellular solids: structure and properties*. Cambridge University Press, Cambridge, 1999.

31. Carter D, Hayes W, Schurman D. Fatigue life of compact bone–ii. effects of microstructure and density. *Journal of Biomechanics* 1976; **9**(4):211 – 214, IN1–IN3, 215–218, doi:10.1016/0021-9290(76)90006-3.

32. Nazarian A, Müller R. Time-lapsed microstructural imaging of bone failure behavior. *Journal of Biomechanics* 2004; **37**(1):55 – 65, doi:10.1016/S0021-9290(03)00254-9.

33. de Giorgi M, Carofalo A, Dattoma V, Nobile R, Palano F. Aluminium foams structural modelling. *Computers & Structures* 2010; **88**(1-2):25 – 35, doi:10.1016/j.compstruc.2009.06.005.

34. Bart-Smith H, Bastawros AF, Mumm DR, Evans AG, Sypeck DJ, Wadley HNG. Compressive deformation and yielding mechanisms in cellular al alloys determined using x-ray tomography and surface strain mapping. *Acta Materialia* 1998; **46**(10):3583 – 3592, doi:10.1016/S1359-6454(98)00025-1.

35. *ASM Handbook Volume 02: Properties and Selection: Nonferrous Alloys and Special-Purpose Materials*. ASM International; 10th edition, 1990.

36. Andrews E, Sanders W, Gibson LJ. Compressive and tensile behaviour of aluminum foams. *Materials Science and Engineering A* 1999; **270**(2):113 – 124, doi:10.1016/S0921-5093(99)00170-7.

37. Maquet V, Martin D, Scholtes F, Franzen R, Schoenen J, Moonen G, Jérôme R. Poly(d,l-lactide) foams modified by poly(ethylene oxide)-block-poly(d,l-lactide) copolymers and a-fgf : in vitro and in vivo evaluation for spinal cord regeneration. *Biomaterials* 2001; **22**(10):1137–1146, doi:10.1016/S0142-9612(00)00357-4.

38. Jonoobi M, Harun J, Mathew AP, Oksman K. Mechanical properties of cellulose nanofiber (cnf) reinforced polylactic acid (pla) prepared by twin screw extrusion. *Composites Science and Technology* 2010; **70**(12):1742 – 1747, doi:10.1016/j.compscitech.2010.07.005.

39. Melchels FP, Bertoldi K, Gabbrielli R, Velders AH, Feijen J, Grijpma DW. Mathematically defined tissue engineering scaffold architectures prepared by stereolithography. *Biomaterials* 2010; **31**(27):6909 – 6916, doi:10.1016/j.biomaterials.2010.05.068.

40. Milan JL, Planell JA, Lacroix D. Computational modelling of the mechanical environment of osteogenesis within a polylactic acid-calcium phosphate glass scaffold. *Biomaterials* 2009; **30**(25):4219 – 4226, doi:10.1016/j.biomaterials.2009.04.026.

41. Léonard A, Guiot L, Pirard JP, Crine M, Balligand M, Blacher S. Non-destructive characterization of deer antlers by x-ray microtomography coupled with image analysis. *Journal of Microscopy* 2007; **225**(3):258–263, doi:10.1111/j.1365-2818.2007.01740.x.

42. Crigel MH, Balligand M, Heinen E. Les bois de cerf : revue de littérature scientifique. *Annales de Médecine Vétérinaire* 2001; **145**(1):25–38.

43. Akhtar R, Daymond MR, Almer JD, Mummery PM. Elastic strains in antler trabecular bone determined by synchrotron x-ray diffraction. *Acta Biomaterialia* 2008; **4**(6):1677 – 1687, doi:10.1016/j.actbio.2008.05.008.

44. Chen PY, Stokes A, McKittrick J. Comparison of the structure and mechanical properties of bovine femur bone and antler of the north american elk (cervus elaphus canadensis). *Acta Biomaterialia* 2009; **5**(2):693 – 706, doi:10.1016/j.actbio.2008.09.011.

45. Currey J. Strain rate dependence of the mechanical properties of reindeer antler and the cumulative damage model of bone fracture. *Journal of Biomechanics* 1989; **22**(5):469 – 475, doi:10.1016/0021-9290(89)90207-8.

46. Krauss S, Fratzl P, Seto J, Currey JD, Estevez JA, Funari SS, Gupta HS. Inhomogeneous fibril stretching in antler starts after macroscopic yielding: indication for a nanoscale toughening mechanism. *Bone* 2009; **44**(6):1105 – 1110,

doi:10.1016/j.bone.2009.02.009.

47. Keaveny TM, Hoffmann PF, Singh M, Palermo L, Bilezikian JP, Greenspan SL, Black DM. Femoral bone strength and its relation to cortical and trabecular changes after treatment with pth, alendronate, and their combination as assessed by finite element analysis of quantitative ct scans. *Journal of Bone and Mineral Research* 2008; **23**(12):1974–1982, doi:10.1359/jbmr.080805.

48. Varga P, Baumbach S, Pahr D, Zysset PK. Validation of an anatomy-specific finite element model of colle's fracture. *Journal of Biomechanics* 2009; **42**:1726 – 1731, doi:10.1016/j.jbiomech.2009.04.017.